Journal of Magnetic Resonance 320 (2020) 106848

Contents lists available at ScienceDirect

Journal of Magnetic Resonance

journal homepage: www.elsevier.com/locate/jmr

Buffer effects on site directed Cu^{2+}-labeling using the double histidine motif

Austin Gamble Jarvi, Joshua Casto, Sunil Saxena *

Department of Chemistry, University of Pittsburgh, Pittsburgh, PA 15260, USA

ARTICLE INFO

Article history:
Received 5 August 2020
Revised 25 September 2020
Accepted 7 October 2020
Available online 9 October 2020

Keywords:
EPR
Spin labeling
Buffer effects
DEER
ESEEM

ABSTRACT

The double histidine, or dHis, motif has emerged as a powerful spin labeling tool to determine the conformations and dynamics, subunit orientation, native metal binding site location, and other physical characteristics of proteins by Cu^{2+}-based electron paramagnetic resonance. Here, we investigate the efficacy of this technique in five common buffer systems, and show that buffer choice can impact the loading of Cu^{2+}-NTA into dHis sites, and more generally, the sensitivity of the overall technique. We also present a standardized and optimized examination of labeling of the dHis motif with Cu^{2+}-NTA for EPR based distance measurements. We provide optimal loading procedures, using representative EPR and UV/Vis data for each step in the process. From this data, we find that maximal dHis loading can be achieved in under 30 min with low temperature sample incubation. Using only these optimal procedures, we see up to a 28% increase in fully labeled proteins compared to previously published results in N-ethylmorpholine. Using both this optimized procedure as well as a more optimal buffer, we can achieve up to 80% fully loaded proteins, which corresponds to a 64% increase compared to the prior data. These results provide insight and deeper understanding of the dHis Cu^{2+}-NTA system, the variables that impact its efficacy, and present a method by which these issues may be mitigated for the most efficient labeling.

1. Introduction

Over the past several decades, electron paramagnetic resonance (EPR) has garnered significant attention as a powerful technique for the measurement of structure and dynamics of biomolecules [1]. A vital component behind the success of EPR is the advent of site-directed spin labeling (SDSL), which enables the positioning of an EPR-active moiety in a desired position within a biomolecule [2]. Single spin labels placed in a macromolecule enable the EPR measurement of site-specific dynamics, solvent accessibility, and secondary structure [3]. By placing two or more labels within a macromolecule, EPR may be used to measure point-to-point distances between the labels, typically within the range of 2–8 nm, although distances up to 16 nm have been measured with full protein deuteration [4,5]. Such distance constraints are used to monitor induced conformational changes [6-17], determine quaternary structural assembly in protein–protein [18–23] and protein-nucleic acid complexes [24–28], probe substrate binding [29–31], and identify native metal coordination sites [32–34].

For proteins, SDSL EPR has most commonly employed nitroxide based spin labels that are attached to the macromolecule via disulfide bonding with free cysteine residues [35]. One significant drawback of these spin labels is that a highly flexible sidechain is often needed in order to tether the EPR-active probe to the macromolecular backbone. Consequently, the inherent fluctuations of the side chain obfuscate the measurement of biologically relevant properties, such as structural constraints and conformational fluctuations of the protein [36,37]. Significant strides have been made to develop bifunctional labels [38-41] that provide more rigidity, but such methods remain reliant on complex synthetic schemes, post-expression synthetic modification, or cysteine attachment, which prevents implementation in protein systems with functional cysteine residues.

In response to these limitations, we have developed a rigid Cu^{2+}-based spin label, the double histidine (dHis) motif [42–44]. This labeling scheme relies on the specific placement of two histidine residues located at positions i to i + 2 for β-sheets, and i to i + 4 for α-helices within a protein. The dHis motif is then used to specifically and rigidly coordinate a Cu^{2+} complex.

The dHis label has produced EPR distance distributions significantly narrower than common spin labels, enabling the efficient deduction of relevant biophysical information, such as

* Corresponding author.
E-mail address: sksaxena@pitt.edu (S. Saxena).

https://doi.org/10.1016/j.jmr.2020.106848
1090-7807/

distinguishing between protein conformations [45] monitoring conformational changes [16], assessing three-dimensional protein arrangement, which has implications for protein–protein and protein-DNA interactions, quaternary structural arrangement, and native metal binding site location [46], as well as determining the relative orientation of protein subunits [47]. In addition, lineshape analysis of the room temperature continuous wave EPR spectrum of the Cu^{2+}-labeled protein provides a new way to directly measure site-specific backbone dynamics at both α-helical and β-sheet sites [48].

However, Cu^{2+} forms complexes easily with many ligands, and therefore there are additional considerations in the implementation of the dHis motif that are not present with nitroxide labeling. First, Cu^{2+} may experience interactions with certain amino acid sidechains [49], leading to non-specific coordination. This complication is mitigated by labeling with Cu^{2+} complexed to nitrilotriacetic acid (NTA) rather than a Cu^{2+} salt [44]. The ligand, NTA, occupies four of the six coordination sites of Cu^{2+}, leaving two sites open for *cis*-coordination to two histidine sidechains, and has been shown to effectively prevent nonspecific binding of Cu^{2+} elsewhere in the protein. However, besides the protein, the solvent presents an additional source of competition for Cu^{2+}-NTA binding to a dHis site [50]. Many buffers commonly used with protein systems have the potential to interact with Cu^{2+} complexes, which can hinder the efficient labeling of the dHis mutated protein.

These considerations may make adoption of the dHis motif non-intuitive. To ameliorate these issues, we present herein two contributions to aid in the widespread use of dHis based labeling. We present a systematic investigation of Cu^{2+}-NTA labeling of dHis modified proteins in five commonly used buffer systems. We use EPR and UV/Vis assays to determine the efficiency of labeling in each buffer environment to highlight the considerations one must make when applying this technique to any protein. Second, we offer a step-by-step protocol of the preparation of the Cu^{2+}-NTA complex and the labeling of dHis mutated proteins, along with representative EPR and UV/Vis experimental controls to provide the expected results and ensure proper labeling. The work presented herein will enable the easier adoption of this technique and promote its widespread use throughout the broader scientific community.

2. Experimental

2.1. Preparation of Cu^{2+} and NTA stock solutions

The preparation for the Cu^{2+}-NTA stock was adapted from prior literature [51], and is included here for ease of referencing. To begin, we first adjusted the pH of an aliquot of standard deionized water to pH 12. Throughout this work, all pH adjustment was achieved by the addition of NaOH to increase pH or HCl to decrease pH. We then dissolved our crystalline NTA (99%, Acros Organics) into the pH 12 deionized water to achieve a concentration of 100 mM NTA. As the solvation of the NTA alters the pH of the solution, continued monitoring and adjustment of the pH may be necessary to ensure the NTA completely dissolves. Next, we prepared a separate buffer solution of 0.1 M MOPS and 0.1 M NaCl in deionized water. This buffer solution was pH adjusted to pH 7.0. We then took an aliquot of the 100 mM NTA solution and diluted it to 3 mM in the MOPS buffer solution. This solution is referred to as our NTA stock solution. We then prepared a Cu^{2+} solution. We first took a new aliquot of deionized water and adjusted its pH to 2.0. We then dissolved $CuSO_4{\cdot}5H_2O$ in that deionized water to a concentration of 3 mM $CuSO_4$. This solution is referred to as our Cu^{2+} stock solution.

2.2. EPR measurements

All experiments were performed on a protein containing two dHis sites as would be usual for distance measurements. Plasmid mutagenesis, and protein expression and purification for all protein mutants were performed using standard procedures [42,52,53]. Protein samples were stored in 150 mM NaCl and 50 mM sodium phosphate buffer at pH 6.5 at 4 °C for up to a week or flash frozen with 20% v/v glycerol and stored indefinitely at −80 °C. The frozen protein was passed through five HiTrap 5 mL desalting columns into the above buffer before labeling to remove the glycerol.

EPR samples were prepared in 50 mM of the respective buffer, with 100 μM protein and 200 μM Cu^{2+}-NTA. 20% v/v glycerol was added as a cryoprotectant. Samples were placed in 3 mm I.D. quartz tubes and refrigerated at 4 °C for 35 min, then transferred on ice to be immediately flash frozen in liquid MAPP gas.

Continuous wave (CW) EPR measurements were performed on a Bruker Elexsys E680 CW/FT X-band spectrometer using a Bruker ER4118X-MD5 resonator at 80 K. All CW EPR experiments were run with a center field of 3100 G and a sweep width of 2000 G, a modulation amplitude of 4 G and a modulation frequency of 100 kHz for 1024 data points using a conversion time of 20.48 ms. CW EPR simulations were performed with EasySpin [54].

Three-pulse electron-spin echo envelope modulation (ESEEM) experiments [55] were performed on a Bruker Elexsys E680 CW/FT X-band spectrometer using a Bruker ER4118X-MD4 resonator at 20 K except where noted. A π/2 –t– π/2 – T – π/2 – echo pulse sequence was used. The π/2 pulse length was 16 ns. The first time delay, t, was set to 140 ns and the second time delay, T, was set to 280 ns and was incremented by a step size of 16 ns. All experiments were performed at the magnetic field corresponding to the greatest intensity on the echo-detected field swept spectrum. A four-step phase cycling was employed to filter out unwanted echoes [56]. Data was averaged over three scans. The resultant signal was phase corrected, baseline subtracted and Fourier-transformed using the Bruker Xepr software. The magnitude of the Fourier transformed spectrum is presented.

Four-pulse double electron electron resonance (DEER) measurements [57,58] were performed on a Bruker Elexsys E680 CW/FT X-band spectrometer using a Bruker EN4118X-MD4 resonator at 20 K. Temperature was controlled by an Oxford ITC503 temperature controller and an Oxford CF935 dynamic continuous flow cryostat connected to an Oxford LLT 650 low-loss transfer tube. The pulse sequence used was $(\pi/2)_{v1}$-τ_1-$(\pi)_{v1}$-τ_1 + t-$(\pi)_{v2}$-τ_2-t-$(\pi)_{v1}$-τ_2-echo. The observer $(\pi/2)_{v1}$ and $(\pi)_{v1}$ pulses were 16 ns and 32 ns respectively. The pump $(\pi)_{v2}$ pulse was 14 ns. t was increased by a step size of 10 ns over 128 points. The time domain data was analyzed by Tikhonov regularization. Data acquisition lasted approximately 5–8 h. DEER data was processed using DeerAnalysis2018 [59].

2.3. UV/Vis measurements

UV/Vis experiments at 8° C were performed on a Varian Cary 50 Bio spectrophotometer using a self-masking quartz spectrophotometer cuvette with a 10 mm path length from Starna Cells. UV/Vis spectra were measured from 220 to 600 nm except where noted. All measurements were baseline corrected using a blank of the respective buffer, and were performed in single beam mode. Data was collected with the Cary WinUV software. UV/Vis samples used 1.2 μM protein with 20% v/v glycerol. Data points in the titrations with protein were collected 15 min after adding an aliquot of Cu^{2+}-NTA. Each reported absorbance was corrected for dilution. For the kinetic time scan, each data point was averaged for 5 s, with 10 s in between each collection.

Supplemental UV/Vis titrations were performed at 4 °C on a Thermo Scientific Nanodrop 2000 and analyzed using the Nanodrop 2000 software package. UV/Vis spectra were monitored at 340 nm. Samples contained 3 μM protein and were blanked with their respective buffer.

3. Results and discussion

3.1. UV/Vis determines optimal Cu^{2+} to NTA ratio

For optimal spin labeling of a protein, maximum chelation of Cu^{2+} by the NTA is desired to ensure removal of free Cu^{2+} which can potentially bind non-specifically. To determine the ideal ratio of NTA to Cu^{2+}, we performed a UV/Vis titration of our NTA stock solution into our Cu^{2+} stock solution, shown in Fig. 1. The Cu^{2+} and NTA stock solutions were prepared as described in the Experimental section. This titration was monitored at two wavelengths, 300 nm and 800 nm, which are representative of NTA coordinating to Cu^{2+} [60]. The titration curve for 300 nm, shown in Fig. 1A, plateaus at 1 equivalent of NTA:Cu^{2+}, and the 800 nm curve, shown in Fig. 1B, plateaus around 1.25 equivalents. This plateauing of the UV/Vis signal indicates a maximal chelation of NTA onto the Cu^{2+} at approximately stoichiometric ratios. Therefore, to prepare our Cu^{2+}-NTA stock solution, we mixed equal volumes of the Cu^{2+} stock with the NTA stock. This final solution was pH adjusted to the desired pH. For our experiments, this value is the physiological pH, 7.4.

We then characterized this Cu^{2+}-NTA stock solution by EPR as shown in Fig. 2. These EPR experimental results serve as controls to verify the proper preparation of the Cu^{2+}-NTA stock solution. First, we performed continuous wave (CW) EPR on the stock solution of Cu^{2+}-NTA with 20% v/v glycerol as a cryoprotectant. The CW EPR spectrum in shown in Fig. 2A. The spectrum was simulated to determine the characteristic EPR parameters, $g_{||}$ and $A_{||}$, which can serve as indicators of the Cu^{2+} coordination environment. Notably, the CW EPR spectrum shows no component that can be attributed to free Cu^{2+}, as shown in Fig. 2A, which indicates that all the Cu^{2+}

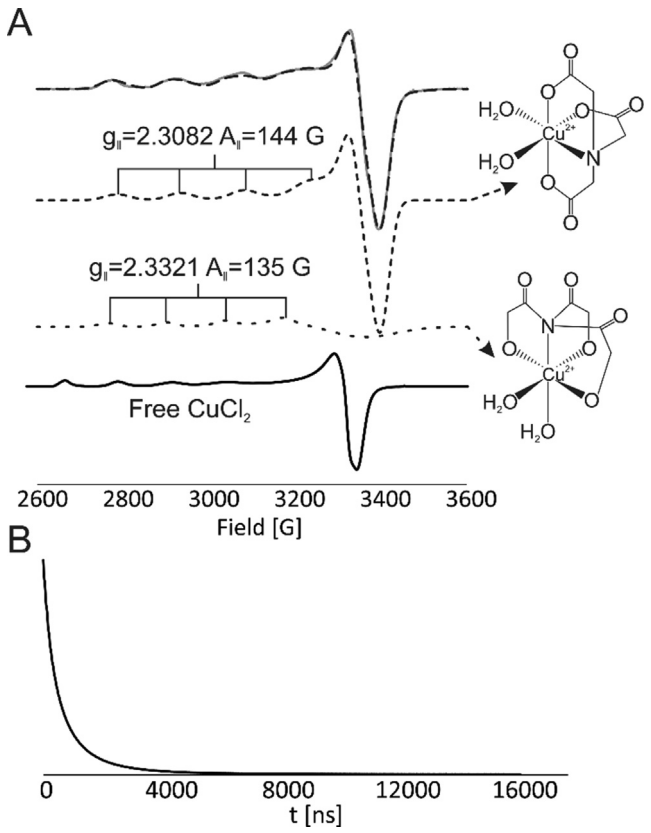

Fig. 2. A) X-Band CW EPR spectrum of the Cu^{2+}-NTA stock. Experimental spectrum of the Cu^{2+}-NTA stock is shown in gray at the top with total simulation shown as a black dashed line. Individual simulation component spectra are shown below in dashed lines with $g_{||}$ and $A_{||}$ parameters noted. The corresponding chemical structures of the proposed coordination modes are shown to the right of the respective spectra. The bottom spectrum shows that of free $CuCl_2$ (in water) for comparison. B) ESEEM signal of the Cu^{2+}-NTA stock performed at 80 K. This data indicates full complexation of Cu^{2+}-NTA, and gives a simple visual assay for proper stock preparation.

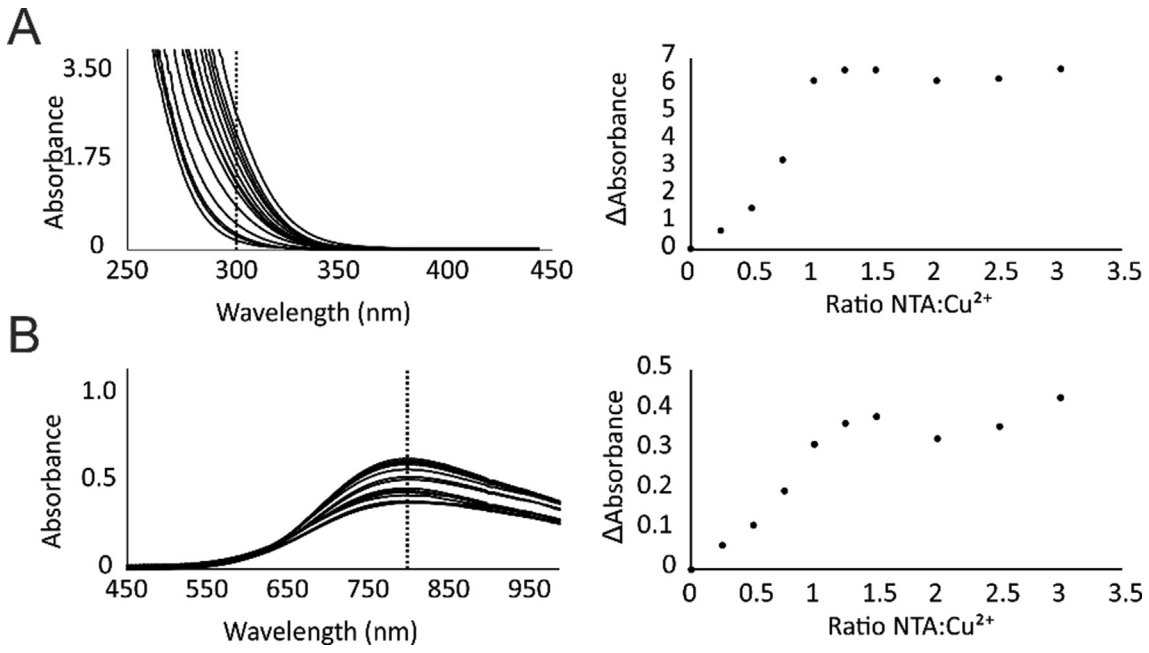

Fig. 1. UV/Vis titration of stock NTA solution into stock $CuSO_4$ solution. This titration was monitored at two separate wavelengths, A) 300 nm and B) 800 nm. The left plots show the experimental UV/Vis spectrum in the particular range that was monitored. The right plots show the change in absorbance on increasing the amount of NTA in the sample. This UV/Vis data indicates that stoichiometric amounts of Cu^{2+} and NTA should be added for optimum chelation.

has indeed coordinated with NTA. The Cu^{2+}-NTA spectrum was fit best with two components, with their $g_{||}$ and $A_{||}$ values noted in Fig. 2A.

The Cu^{2+}-NTA complexes have several possible coordination modes, which may explain the two observed components in the Cu^{2+}-NTA spectrum [61]. The first component, with $g_{||}$=2.3082 and $A_{||}$=144 G, is consistent with a coordination of one nitrogen and three oxygens in the equatorial plane [62]. This component comprises approximately 80% of the total spectrum. The second component displayed a higher $g_{||}$ and a lower $A_{||}$ ($g_{||}$=2.3321 and $A_{||}$=135 G), a trend that is consistent with increasing oxygen coordination [62]. This coordination environment is possible with the nitrogen of the NTA ligand coordinating axially to the Cu^{2+}, with four equatorial oxygens. These proposed coordination modes are illustrated next to their respective EPR spectra in Fig. 2A.

It is well established that Cu^{2+} has high affinity for NTA, with a sub-picomolar apparent dissociation constant, K_d [63]. This high affinity is evident from our CW spectra in Fig. 2A, which showed complete complexation of the Cu^{2+} with the NTA ligand. Note that the interaction of Cu^{2+} with two imidazole ligands is likewise well studied, with a K_d of 270 μM [64]. This affinity suggests a relatively weak binding of free Cu^{2+} to two histidines. However, the Cu^{2+}-NTA complex with two histidine residues shows a K_d of 100 μM, a factor of approximately 3 better than Cu^{2+} alone [65]. This data supports the implementation of NTA with the dHis motif.

We next performed electron spin echo envelope modulation (ESEEM) on the Cu^{2+}-NTA stock. ESEEM is sensitive to nuclear spins within 3–8 Å of the Cu^{2+} electron spin, which are identified by modulations in the time domain signal. This signal is shown in Fig. 2B. Notably, there are no visible nuclear modulations. This result is expected, as the Cu^{2+}-NTA should only have directly coordinated nitrogen atoms, which are not detected due to the finite bandwidth of the pulses in the experiment. Note that we performed this and all following ESEEM experiments in such a manner to filter out nuclear modulations arising from interactions with hydrogen in the solvent [66].

3.2. UV/Vis assesses optimal ratio of Cu^{2+}-NTA to protein for distance measurements

The dHis motif, as shown in Fig. 3A, requires the incorporation of two histidine residues placed in strategic locations within the protein. The dHis motif has been successfully used in both α-helices and β-sheets. For β-sheets, as shown in Fig. 3B, the histidine residues are placed in an i, i + 2 arrangement. This allows both histidine residues to face the same plane of the β-sheet in order to coordinate the Cu^{2+}-NTA. For α-helices, the histidine residues should be positioned in i, i + 4 positions. In this arrangement, the two histidine residues point the same direction from the helix for Cu^{2+}-NTA coordination. In principle, the dHis motif can make use of native histidine residues, which can simplify the mutation process. As with other spin-labeling methods, it is advantageous to position the dHis site in a solvent exposed region of the protein to enable efficient loading of the Cu^{2+}-NTA into the site. Additionally, Cu^{2+}-NTA shows a higher affinity for α-helical dHis sites [44,67].

Incorporation of non-native histidines was achieved through standard mutagenesis, protein expression and purification procedures [42,52,53]. In this work, all results were obtained on a tetramutant of the immunoglobulin binding domain of protein G (GB1) with dHis sites at a β-sheet, 15H/17H, and an α-helical site, 28H/32H. This protein system is well characterized and has been used for much of the development of the dHis motif [42–44,46,47].

We next used UV/Vis titrations to determine the optimal amount of the Cu^{2+}-NTA for labeling proteins. Such considerations are important because excess Cu^{2+}-NTA contributes to the background signal in pulsed dipolar spectroscopy which leads to a loss of sensitivity towards the intramolecular dipolar interaction. Cu^{2+}-NTA stock was titrated into a sample containing 1.2 μM GB1 in a buffer of 50 mM sodium phosphate buffer at pH 7.4 (Fig. 4A), and a sample in 50 mM N-ethylmorpholine (NEM) at pH 7.4 (Fig. 4B). Both samples contained 20% v/v glycerol to examine binding under conditions typically used for low-temperature EPR. Sodium phosphate was chosen as a simple representative buffer because previous work has determined the K_d of Cu^{2+}-NTA to dHis in this buffer system [67]. NEM was used as it has been the default buffer employed in most work involving the dHis motif thus far. Additionally, the temperature was maintained at 8 °C for the duration of these titrations. Note that the binding of Cu^{2+}-NTA to dHis is exothermic and lower temperatures ensure higher binding [67]. The UV/Vis titrations were monitored at 340 nm, which corresponds to a metal-to-ligand charge transfer band [68]. The experimental changes in absorption, corrected for dilution, are plotted as black circles.

We then fit the data using a 1:1 (dHis:Cu^{2+}-NTA) binding model, detailed in Equation (1). [69,70] This model assumes that both α-helix and β-sheet sites experience identical binding affinities to the Cu^{2+}-NTA. While we know this is not the case [44,67], such an assumption simplifies our model, and still provides an 'average' apparent dissociation constant, K_d, of the two sites with reasonable accuracy, as is discussed below.

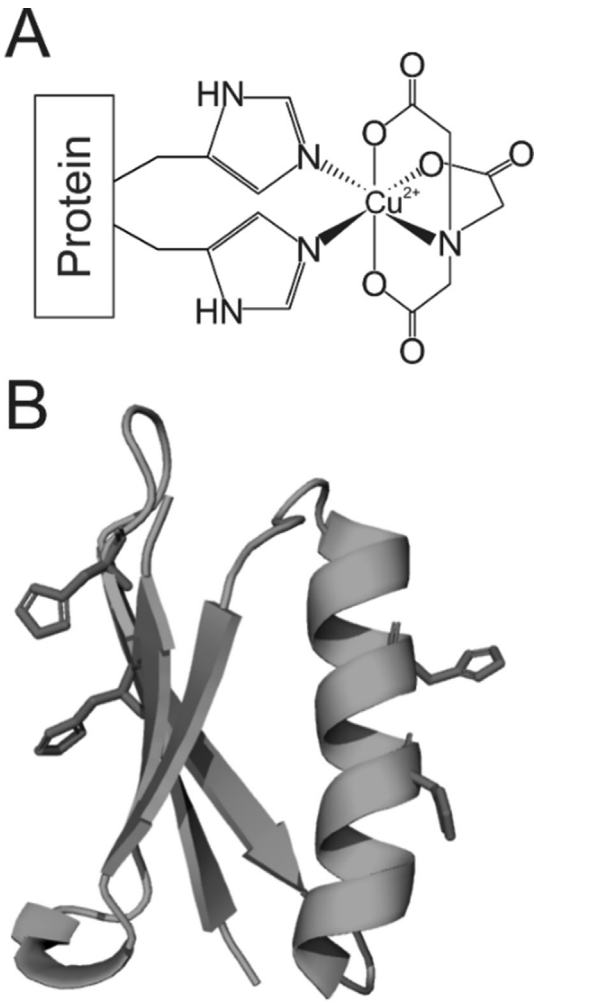

Fig. 3. A) Chemical structure of the dHis Cu^{2+}-NTA labeling motif. B) Molecular model (PDB: 4WH4) of a model protein including a β-sheet site and an α-helical site showing the full histidine side chains for illustration.

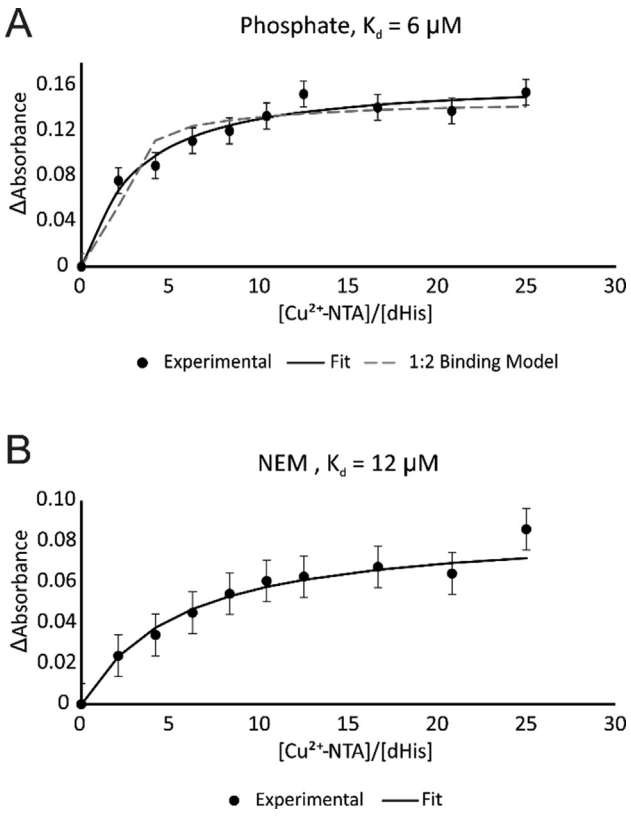

Fig. 4. UV/Vis titrations of Cu^{2+}-NTA stock into tetramutant 15H/17H/28H/32H GB1 at 8 °C. The titrations were monitored at 340 nm. A) Titration performed in 50 mM sodium phosphate buffer, pH 7.4. Black circles show experimental ΔAbsorbance values. The fit to the experimental data using a 1:1 (dHis:Cu^{2+}-NTA) binding model is shown as the solid black line. A fit to the data using a 1:2 (GB1:Cu^{2+}-NTA) with the α-helix and β-sheet K_d values previously determined by ITC is shown as the gray dashed line. B) Titration performed in 50 mM NEM buffer, pH 7.4, with a 1:1 binding model fit as above. This data shows slight effects of buffer on the apparent dissociation constant of Cu^{2+}-NTA to dHis.

$$\Delta Abs = \frac{Abs_{\Delta HG}}{2}\left[[H_0]+[G_0]+K_d-\sqrt{\left([H_0]+[G_0]+K_d\right)^2+4[H_0][G_0]}\right] \quad (1)$$

In Equation (1), $[H_0]$ is the initial concentration of dHis sites, $[G_0]$ is the initial concentration of Cu^{2+}-NTA, K_d is the 'average' apparent dissociation constant, and $Abs_{\Delta HG}$ is the contribution to the UV/Vis absorbance resulting from the coordination of Cu^{2+}-NTA to dHis. In this equation, K_d and $Abs_{\Delta HG}$ are unknowns. The equation was fit to the data by minimizing the RMSD between the experimental ΔAbs and the calculated ΔAbs by changing the K_d and $Abs_{\Delta HG}$. Multiple starting seed values for K_d and $Abs_{\Delta HG}$ were used to avoid the RMSD minimization getting stuck in local minima. By this method, we calculate that K_d = 12 ± 5 μM in NEM and K_d = 6 ± 2 μM in sodium phosphate buffer. The uncertainty in these measurements was estimated from the error in the individual data points.

Previous work determined the K_d values of both α-helix and β-sheet dHis sites in GB1 at room temperature in 50 mM phosphate buffer by isothermal titration calorimetry (ITC) [67]. This work determined the α-helix K_d = 5 μM and the β-sheet K_d = 42 μM at room temperature (25 °C), as well as their respective ΔH values. Using the Van't Hoff equation (Equation (2)), we can extrapolate these K_d values at 8 °C as used in our titrations, under the assumption that the ΔH does not change significantly in the range of temperatures used:

$$ln\left(\frac{K_2}{K_1}\right)=\frac{\Delta H^{\varnothing}}{R}\left(\frac{1}{T_2}-\frac{1}{T_1}\right) \quad (2)$$

This equation results in an α-helix K_d = 2 μM and a β-sheet K_d = 16 μM at 8 °C. For the simplest and most direct comparison, we have averaged these two values to $K_{d,avg}$ = 9 μM. This $K_{d,avg}$ value is similar to our experimentally calculated value (K_d = 6 ± 2 μM). However, for a more accurate comparison, we then used the two separate α-helix and β-sheet K_d values to plot a curve following a 1:2 (GB1:Cu^{2+}-NTA) binding model. Such a model takes into account differences in affinity of each of the two distinct dHis sites within a single protein, and is described as:[69]

$$\Delta Abs = \frac{Abs_{\Delta HG1}[H_0]K_\alpha[G]+Abs_{\Delta HG2}[H_0]K_\alpha K_\beta[G]^2}{1+K_\alpha[G]+K_\alpha K_\beta[G]^2} \quad (3)$$

Where $Abs_{\Delta HG1}$ is the contribution to the UV/Vis absorbance resulting from the coordination of Cu^{2+}-NTA to and α-helix dHis site, $Abs_{\Delta HG2}$ is the contribution to the UV/Vis absorbance resulting from the coordination of Cu^{2+}-NTA to and β-sheet dHis site, K_α and K_β are the K_d values for the α-helix and β-sheet sites respectively, and [G] is the concentration of free Cu^{2+}-NTA. [G] is calculated as a function of knowns by:[69]

$$0=[G]^3(K_\alpha K_\beta)+[G]^2(K_\alpha(2K_\beta[H_0]-K_\beta[G_0]+1)) + [G](K_\alpha([H_0]-[G_0])+1)-[G_0] \quad (4)$$

The $Abs_{\Delta HG1}$ and $Abs_{\Delta HG2}$ were determined with RMSD minimization as above, and the 1:2 binding fit is plotted as the gray dashed line in Fig. 4A. This more complete model is slightly deviated from our experimental values, but still provides a close fit to the data. The similarity between this fit and our experimental fit using an 'average' K_d suggests that our data is in agreement with the previous ITC data, and the treatment of this system as a 1:1 (dHis:Cu^{2+}-NTA) binding model is sufficient to qualitatively analyze binding for our purposes.

We next repeated the titration in 50 mM NEM buffer, shown in Fig. 4B, and fit the experimental data. The NEM titration provided an average K_d of 12 ± 5 μM (compared to 6 ± 2 μM for the phosphate buffer). This result is an indication of the impact of buffer on the apparent K_d. The data suggests a slightly greater loading of Cu^{2+}-NTA to dHis sites in the sodium phosphate as compared to NEM buffer.

After determining the K_d, we used the calculated values to estimate the amount of dHis loading we could expect in our EPR samples to determine the optimal number of equivalents of Cu^{2+}-NTA to use. Fig. 5A and B show plotted the percentage of dHis sites loaded in a sample of 100 μM protein at added Cu^{2+}-NTA equivalents from 0 to 3 (as the dHis binding is effectively saturated past this point) in phosphate buffer (5A) and NEM buffer (5B). The values plotted were calculated using:[69]

$$[HG]=\frac{1}{2}\left[[H_0]+[G_0]+K_d-\sqrt{\left([H_0]+[G_0]+K_d\right)^2+4[H_0][G_0]}\right] \quad (5)$$

Where [HG] is the concentration of dHis-bound Cu^{2+}-NTA. The K_d used for these calculations was as determined by our titrations, with K_d = 6 ± 2 μM for phosphate and K_d = 12 ± 5 μM for NEM. From the plots in Fig. 5A and B, we see that greater than 80% of the dHis sites are loaded at 1 equivalent and higher Cu^{2+}-NTA in both phosphate and NEM buffer. However, for EPR distance methods, the presence of excess free Cu^{2+}-NTA degrades the signal, and so the amount of free Cu^{2+} in the sample should be minimized. To this end, Fig. 5C and D shows the component percentages of free Cu^{2+}-NTA and dHis-bound Cu^{2+}-NTA for 0 to 3 equivalents of added Cu^{2+}-NTA for phosphate and NEM buffers using their calculated K_d

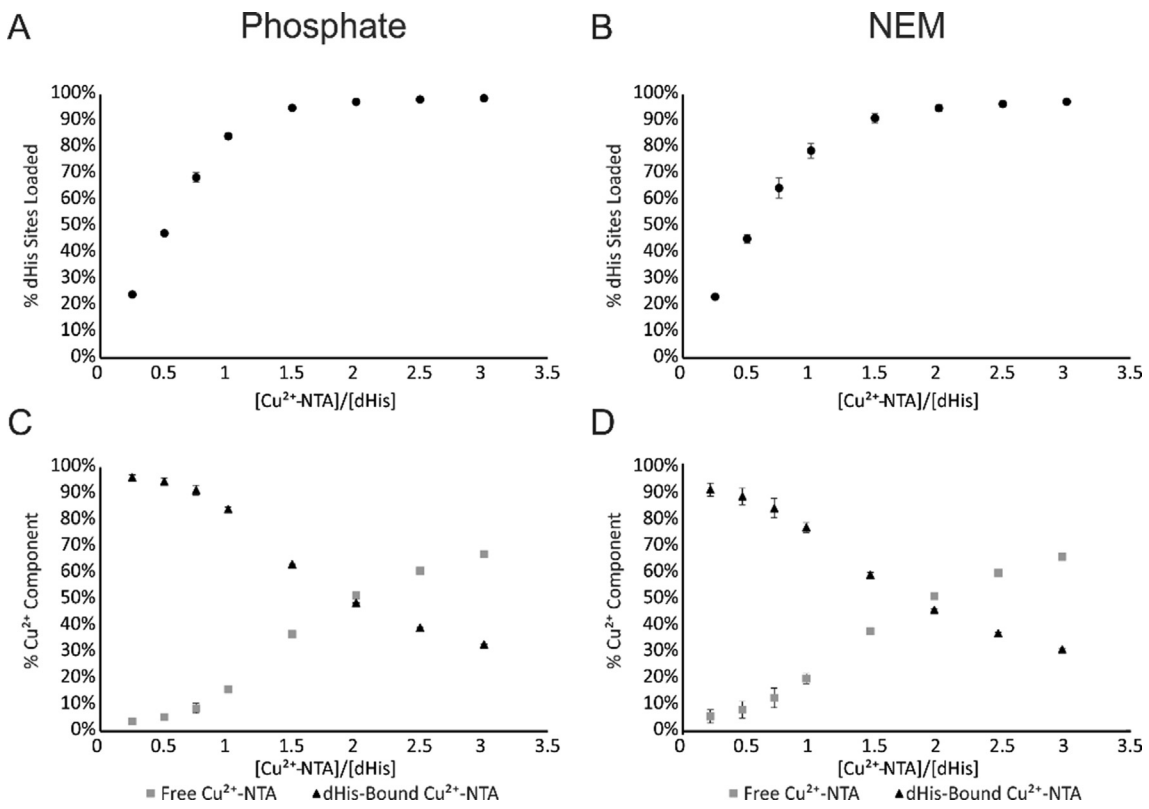

Fig. 5. (A) A plot of the expected percentage of loaded dHis sites for a 100 μM protein sample as estimated by our calculated K_d = 6 ± 2 μM in phosphate buffer for 0 to 3 equivalents of added Cu^{2+}-NTA. (B) A plot of the expected percentage of loaded dHis sites for a 100 μM protein sample as estimated by our calculated K_d = 12 ± 5 μM in NEM buffer for 0 to 3 equivalents of added Cu^{2+}-NTA. (C) A plot of the component percentages for a 100 μM protein sample as estimated by our calculated K_d = 6 ± 2 μM in phosphate buffer for 0 to 3 equivalents of added Cu^{2+}-NTA. (D) A plot of the component percentages for a 100 μM protein sample as estimated by our calculatedK_d = 12 ± 5 μM in NEM buffer for 0 to 3 equivalents of added Cu^{2+}-NTA. Free Cu^{2+}-NTA is plotted as gray squares. dHis-Bound Cu^{2+}-NTA is plotted as black triangles. These plots suggest stoichiometric addition of Cu^{2+}-NTA to dHis lead to between 80% loading and less than 20% free Cu^{2+}-NTA.

values. Again, the two buffers show little difference, with both maintaining less than 20% free Cu^{2+}-NTA below 1 equivalent of added Cu^{2+}-NTA.

We also performed similar measurements at 4 °C (Fig. S2). A temperature of 4 °C was chosen for incubation as it is a common temperature at which typical refrigerators are maintained and is therefore easily accessible. These data are provided in Fig. S2 of the Supporting Information. Taking all data together, we see that stoichiometric loading, or 1 equivalent of Cu^{2+}-NTA per dHis site present in the protein, achieves a balance of achieving >80% loading of the dHis sites, while keeping the total percentage of free Cu^{2+}-NTA in the sample below 20%.

We then performed a kinetic time scan to determine the details of sample incubation for optimal Cu^{2+}-NTA coordination. Two equivalents of Cu^{2+}-NTA were added to the protein sample, or 1 equivalent of Cu^{2+}-NTA per dHis site, and we monitored the UV/Vis absorbance of a protein sample at 340 nm. The data were obtained at 8 °C. The sample was prepared in 50 mM NEM buffer, and was prepared as it would be for distance measurements, with 20% v/v glycerol. The sample was stirred for 5 s before loading into the cuvette and then into the spectrophotometer. The total dead time from addition of the Cu^{2+}-NTA into the protein sample to initial data collection was ~15 s. The results of this kinetic scan are shown in Fig. 6. From this data, we determined that maximal loading of the dHis sites occurs after ~25 min of low temperature sample incubation, and 50% labeling is achieved after approximately 12-minutes of incubation. These results show that for surface accessible sites, incubation for 30–40 min should suffice to achieve maximal loading even with the slight differences in binding between buffers. An additional buffer was used to verify this assumption, and the data is shown in Fig. S1.

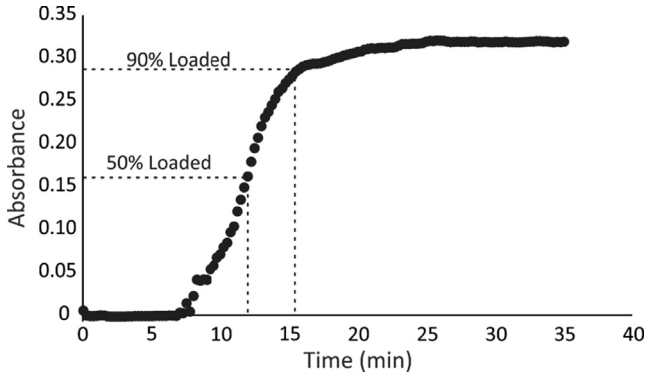

Fig. 6. UV/Vis time scan at 340 nm to assess the amount of incubation necessary for complete coordination of the Cu^{2+}-NTA with the dHis modified protein. The system was held at 8 °C for the duration. This curve shows that maximum dHis loading is achieved in less than 30 min at low temperature.

3.3. Buffer choice affects loading of Cu^{2+}-NTA to dHis

After determining the ideal ratio and incubation time for the Cu^{2+}-NTA dHis samples, we characterized the resulting samples by CW EPR. The data are shown in Fig. 7. First, we performed CW EPR on samples of 100 μM Cu^{2+}-NTA stock in 50 mM of one of five commonly used buffers: MOPS (3-N-morpholinopropanesulfonic acid), Sodium Phosphate, HEPES (4-(2-hydroxyethyl)-1-piperazi

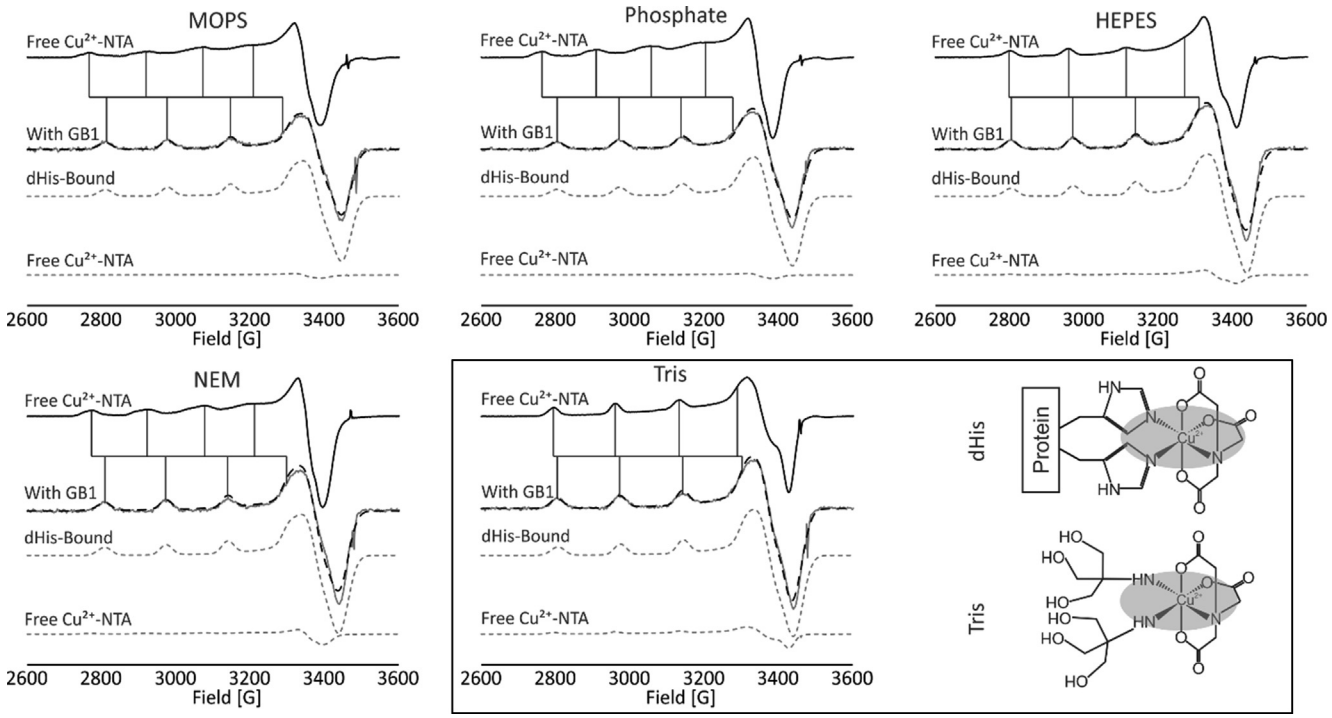

Fig. 7. CW EPR spectra of free Cu^{2+}-NTA, and 15H/17H/28H/32H GB1 in each buffer, as labeled. The top spectrum in each frame is the free Cu^{2+}-NTA, shown as a solid black line. The middle spectrum is the GB1 sample, with the experimental spectrum in solid gray and a simulation in black dashed lines. Vertical lines are drawn tracing the $A_{\|}$ splitting in both spectra to emphasize the spectral shifts on addition of protein. The bottom two spectra, shown in dashed gray lines, are the dHis bound and free Cu^{2+}-NTA spectra used in the simulation. This figure emphasizes the clear visual cue that indicates Cu^{2+}-NTA to dHis binding in all but the Tris sample.

neethanesulfonic acid), NEM, and Tris (2-Amino-2-(hydroxyme thyl)propane-1,3-diol), all pH 7.4. These free Cu^{2+}-NTA spectra are shown as the top spectra in each frame in Fig. 7, as labeled. We then prepared samples of 100 μM protein with 2 equivalents of Cu^{2+}-NTA (1 equivalent per dHis site) in 50 mM of each buffer. Samples were incubated for 35 min at 4 °C before being frozen.

Fig. 7 shows the experimental CW-EPR spectra of Cu^{2+}-NTA-protein compared to the spectra of the free Cu^{2+}-NTA in each buffer. Immediately apparent from these results are clear spectral shifts upon the addition of protein in all but the Tris sample, specifically in the $g_{\|}$ region of the spectra. The splitting due to $A_{\|}$ vary by as much as 40–80 G between the free Cu^{2+}-NTA sample and the sample with protein in phosphate, MOPS, and NEM buffers, and by up to 30 G in HEPES buffer. In the Tris samples however, equivalent $A_{\|}$ splittings varied by only up to 10 G, making the spectral shift difficult to ascertain in the broad Cu^{2+} EPR spectrum. These spectral shifts are often a clear visual indication of proper Cu^{2+}-NTA binding to dHis, and a key assay of the sample preparation. Such spectral shifts result from *cis*-coordination for the two histidine residues leading in an increase in the number of equatorially coordinated nitrogen atoms [62].

On the other hand, the sample prepared in Tris buffer shows a remarkable similarity between the spectrum without protein and the spectrum with protein. This similarity between the dHis-bound and free Cu^{2+}-NTA signal in Tris is indicative of solvent interaction with the Cu^{2+}- NTA, in which two amino nitrogens from the Tris buffer coordinate to the Cu^{2+}-NTA. Such interaction would produce a local coordination environment of the Cu^{2+} that is very similar to that of a Cu^{2+}-NTA coordinated to two histidine residues. A comparison of the coordination environments from these two cases is shown in the boxed region of Fig. 7, with the local Cu^{2+} coordination environment highlighted. This ambiguity makes it difficult to accurately assess the extent of binding of Cu^{2+}-NTA to dHis in Tris buffer from CW EPR data alone.

To estimate the loading of the dHis sites, we performed simulations of each CW EPR spectrum. Two components were required in each case, as anticipated. The first component, labeled as dHis-Bound in Fig. 7, represents Cu^{2+}-NTA that has coordinated to the dHis site. This component was simulated via EasySpin [54], with variable g and A parameters, and component weight. The second component, labeled Free Cu^{2+}-NTA in Fig. 7, is representative of Cu^{2+}-NTA that has not coordinated with a dHis site. For this component, we used the experimental spectrum of the free Cu^{2+}-NTA with a variable weight. The final simulation is a superposition of each component in ratios defined by the component weights. By fitting the g and A parameters of the dHis-Bound component, and the weights of both components, we achieve an overall simulation of the system, shown as the black dashed line overlaid on the experimental protein spectra in each frame of Fig. 7. The results of these simulations – the g and A parameters of the dHis bound component and the percent weights of each component – are listed in Table 1.

From the simulation data, we observe that the choice of buffer does not have significant impact on the g and A parameters of the dHis-bound EPR spectra. The $g_{\|}$ and $A_{\|}$ values are generally consistent across every buffer, with only very slight fluctuations. This result is expected as the dHis-Cu^{2+}-NTA coordination is relatively identical in all buffers. As visualized in Fig. 7, samples in MOPS, phosphate, and NEM buffers show distinctly different $g_{\|}$ and $A_{\|}$ values from free Cu^{2+}-NTA in the same buffers. HEPES showed slightly different parameters, although not as dramatic as the above examples. And finally, the Tris sample showed nearly indistinguishable parameters between the free Cu^{2+}-NTA sample and the sample with protein.

The component ratios show some variance of up to 10%, but these differences are difficult to quantify from CW-EPR alone, due to the large errors. Additionally, the sample in Tris buffer displayed the highest uncertainty in component percentage, as the

Table 1
g and A EPR parameters for dHis-bound components in each buffer, and the percent weights for both dHis-Bound and Free Cu^{2+}-NTA components. The parameters for free Cu^{2+}-NTA for comparison are: In MOPS, Phosphate, and NEM: $g_{\|}$ = 2.308 $A_{\|}$ = 144 G. In HEPES: $g_{\|}$ = 2.282 $A_{\|}$ = 158 G. In Tris: $g_{\|}$ = 2.268 $A_{\|}$ = 164 G.

Buffer	$g_{\perp}$	$g_{\|}$	$A_{\perp}$ (G)	$A_{\|}$ (G)	% dHis-Bound	% free Cu^{2+}-NTA
MOPS	2.051	2.268	5	164	95 ± 5	5 ± 5
Phosphate	2.051	2.267	5	165	95 ± 5	5 ± 5
HEPES	2.051	2.268	5	164	90 ± 8	10 ± 8
NEM	2.051	2.268	5	164	89 ± 5	11 ± 5
Tris	2.051	2.272	5	165	85 ± 15	15 ± 15

similarity of the free Cu^{2+}-NTA and dHis-bound spectra in Tris make this quantification difficult. These factors make further assays of loading necessary. On the other hand, our CW EPR results agree with our estimated loading calculated from the $K_d$values, in which each 100 μM EPR sample experiences upwards of 80% loading of the dHis sites.

We further assessed the binding of Cu^{2+}-NTA to the dHis sites and the impact of the buffer choice using ESEEM, shown in Fig. 8. The ESEEM signals offer additional insight into the loading efficiency of Cu^{2+}-NTA to dHis. ESEEM is sensitive to the imidazole nitrogens found in histidine coordination (cf. Fig. 3), resulting in the characteristic modulations exhibited in Fig. 8A. However, free Cu^{2+}-NTA lacks this imidazole coordination, and as such displays no modulations, merely a featureless decay, as seen previously in Fig. 2B. When both dHis-bound Cu^{2+}-NTA and free Cu^{2+}-NTA are present in a sample, the resulting ESEEM signal is a superposition of these modulating and featureless signals. With increasing free Cu^{2+}-NTA in a given sample, the featureless signal leads to a shallower modulation in the overall ESEEM signal. The depth or shallowness of the modulation can be quantified by the modulation depth, k, and is shown in the inset in Fig. 8A [71]. Through this k parameter, the extent of Cu^{2+} coordination to the imidazole nitrogen of histidine can be monitored. [43,72,73]

Notably, all samples displayed modulations of near identical frequency, but because the percentages of dHis-bound Cu^{2+}-NTA and free Cu^{2+}-NTA differ across buffers, the ESEEM modulations differ in the magnitude of these modulations. We calculated the ESEEM modulation depths for each buffer using the first major modulation that begins around 1000 ns, shown in Table 2. The error was estimated from the noise level of the time domain ESEEM signal. From this data, we see that using MOPS and phosphate buffers produce the deepest modulations, indicating the most efficient loading of the dHis sites with Cu^{2+}-NTA. NEM and HEPES buffers produced comparable, if slightly lower, modulation depths, while Tris buffer produced the lowest modulation depth. These results correspond well with the calculated component ratios from CW EPR, in which MOPS and phosphate buffers exhibited the highest dHis loading, with HEPES and NEM only slightly lower, and Tris buffer as the lowest.

Table 2
Calculated ESEEM modulation depths for the Cu^{2+}-NTA with GB1 in various buffers.

Buffer	Modulation Depth (k)
MOPS	27 ± 1%
Phosphate	26 ± 1%
HEPES	24 ± 1%
NEM	24 ± 1%
Tris	20 ± 1%

Fig. 8B shows the ESEEM spectra. In all five buffer systems we see a clear and characteristic spectrum of imidazole nitrogen coordination, typified by a broad transition around 5 MHz, called the double quantum (DQ) peak, and a set of 3 transitions below 3 MHz, called the nuclear quadrupole interactions (NQI) [72,73]. These transitions are all resolved in the Fourier transformed spectra, and dashed lines in Fig. 8B trace each peak through every buffer system. This ESEEM data clearly indicates that the Cu^{2+}-NTA is coordinating to the dHis sites in all buffer systems, albeit with different loading efficiencies.

We lastly performed DEER distance measurements on each sample, as shown in Fig. 9. The DEER distance distribution provides perhaps the most obviously useful structural data. From Fig. 9, we see that regardless of buffer, each DEER produced a distance distribution centered on 2.3 nm, with a FWHM of 0.2 nm. This distribution is consistent with previous work [44].

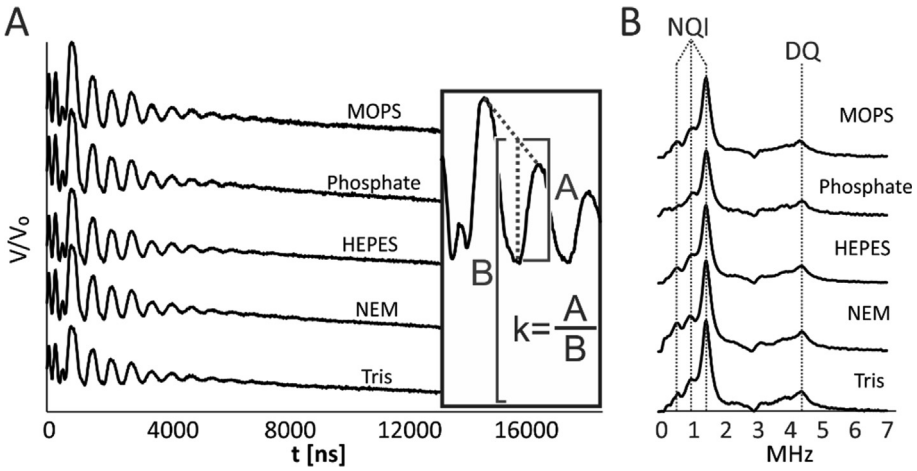

Fig. 8. (A) Time domain ESEEM signals for 2:1 Cu^{2+}-NTA:GB1 in their respective buffers. Modulation depth calculations utilized the second major modulation around 1500 ns. (B) Fourier Transformed ESEEM signals for each sample in its respective buffer. These data show characteristic imidazole nitrogen coordination, indicating proper coordination of Cu^{2+}-NTA to dHis.

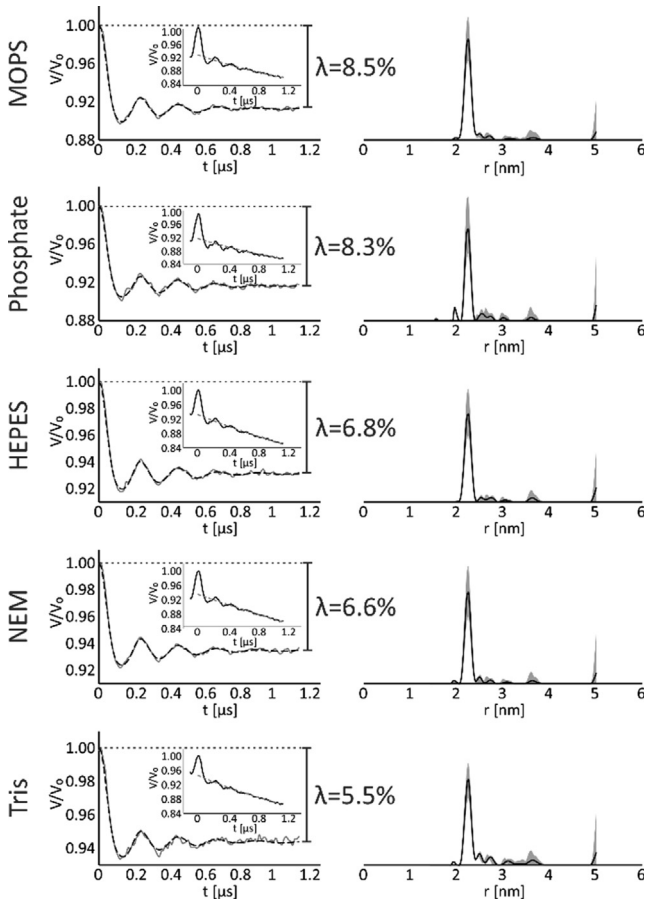

Fig. 9. DEER data for 100 μM 15H/17H/28H/32H GB1 with 2 equivalents of Cu^{2+}-NTA, incubated at 4 °C for 35 min in each of the five buffer systems. The left column shows the background subtracted time domain signal in gray with Tikhonov regularized fit in black dashed lines. The inset shows the raw time domain signal, with the gray dashed line indicating the background. Modulation depth parameters, λ, are noted. The right column shows the distance distributions obtained using Tikhonov regularization, with gray shading indicating the uncertainty of analysis. The data clearly show the impact of buffer on the sensitivity of the DEER technique.

More importantly, the modulation depth, λ, of the DEER signal provides information on the amount of dHis loading in the sample. The modulation depth is the difference between the maximum signal intensity and the signal intensity at the baseline in a normalized, background subtracted DEER signal. This definition is illustrated in Fig. 9. The modulation depth is sensitive to the number of coupled spins in the species being measured – with a higher proportion of doubly labeled proteins, the modulation depth will increase, whereas with more incomplete loading or a higher amount of free Cu^{2+}-NTA, the modulation depth will decrease. DEER modulation depth for a two-spin system is defined in simplest terms as:[43,44]

$$\lambda = 1 - [f_2(1 - p_b) + f_1] \quad (6)$$

where f_2 is the fraction of doubly labeled species, and f_1 is the fraction of single Cu^{2+} species, which is comprised of both singly labeled GB1 and free Cu^{2+}-NTA. p_b is the probability of the pump pulse exciting a B spin in DEER. p_b is dependent on numerous factors such as magnetic field, microwave frequency, pump pulse shape and length, and the EPR spectrum itself, and can be calculated from the experimental echo detected field swept spectrum of the system [74]. In our analysis we estimated the error in the DEER modulation depth from the noise in the time domain signal. In order to determine the consistency and reproducibility of our modulation depth, we also performed DEER measurements on new sample preparations in phosphate buffer and Tris buffer, as representatives of most and least optimal buffers. These results are shown in Figure S3. From this data, the modulation depths are generally reproducible, although there are slight variations (e.g. 5.7 ± 0.1% for Tris and 7.8 ± 0.4% for phosphate (average ± s.d.)). These differences are likely due to inherent uncertainty in the measurement of concentration and volume during sample preparation.

From the DEER modulation depth and our calculated p_b, we can calculate f_2 and f_1, as:

$$f_1 = 1 - f_2 \quad (7)$$

Doing so for each buffer, we can holistically examine how buffer choice affects dHis loading. The results of these calculation, along with a summary of the quantitative results so far, are shown in Fig. 10.

From all the compiled results in Fig. 10, we can see the consistent results through each experiment to fully inform our understanding of the impacts of sample preparation and buffer choice on the loading of the dHis sites. First, we can compare our DEER results with those performed previously for the Cu^{2+}-NTA system with GB1 in NEM, which reported an f_2 = 0.50 [44]. Our NEM sample, using optimized preparation conditions, achieved an f_2 = 0.64, which corresponds to a 28% increase in f_2. Such an increase in f_2 can lead to significant improvements in DEER sensitivity [75]. Clearly, the optimized conditions of stoichiometric Cu^{2+}-NTA addition and low temperature incubation have major impact on the loading of the dHis sites.

Furthermore, our data indicates that buffer choice can play a role in the overall loading efficiency. If we consider both optimized preparation conditions and the optimal buffer system, our maximum f_2 across all samples is 0.82. This value is a 64% increase in loading efficiency compared to the previously published result [44]. Additionally, our EPR data is consistent across each individual experiment, and the cumulative CW EPR component percentages, ESEEM modulation depths, and DEER species fractions indicate that MOPS and phosphate buffer promote maximal Cu^{2+}-NTA binding, with Tris buffer degrading the loading to the dHis site. It is also of note that relatively small differences in overall dHis loading, as determined from CW EPR, can have much larger impacts on the amount of doubly labeled systems for DEER. While the Tris buffer sample shows only 10% lower total dHis binding from CW EPR, this result translates to a ~ 33% reduction in f_2 (from 0.82 in Phosphate to 0.55 in Tris), and a ~ 35% reduction in modulation depth (from 0.085 in Phosphate to 0.055 in Tris).

Finally, we measured data on a different GB1 mutant to explore the generality of the observed effects of buffer. We prepared a different mutant of GB1, with dHis sites at the same α-helical site, 28H/32H, and a different β-sheet site, 6H/8H, and performed DEER on samples in phosphate buffer and in Tris, to represent the most and least optimal buffers, respectively. The DEER data is shown in Fig. 11. The modulation depth was 5.4% in phosphate buffer and 3.3% in Tris. These data support the result that phosphate buffer promotes higher Cu^{2+}-NTA binding, whereas Tris buffer degrades it.

In general, our EPR results also align with known thermodynamic properties of these buffers and their interactions with Cu^{2+}, as specific data regarding the affinities of the buffers with Cu^{2+}-NTA is not readily available. In broad terms, Tris buffer has a higher affinity to interact with Cu^{2+} ions [76], and likewise displayed the lowest extent of Cu^{2+}-NTA to dHis loading, whereas sodium phosphate buffer, which provided one of the greatest loadings of Cu^{2+}-NTA to dHis also exhibits a notably lower affinity to interact with Cu^{2+} [77,78]. Our EPR results and the supporting ther-

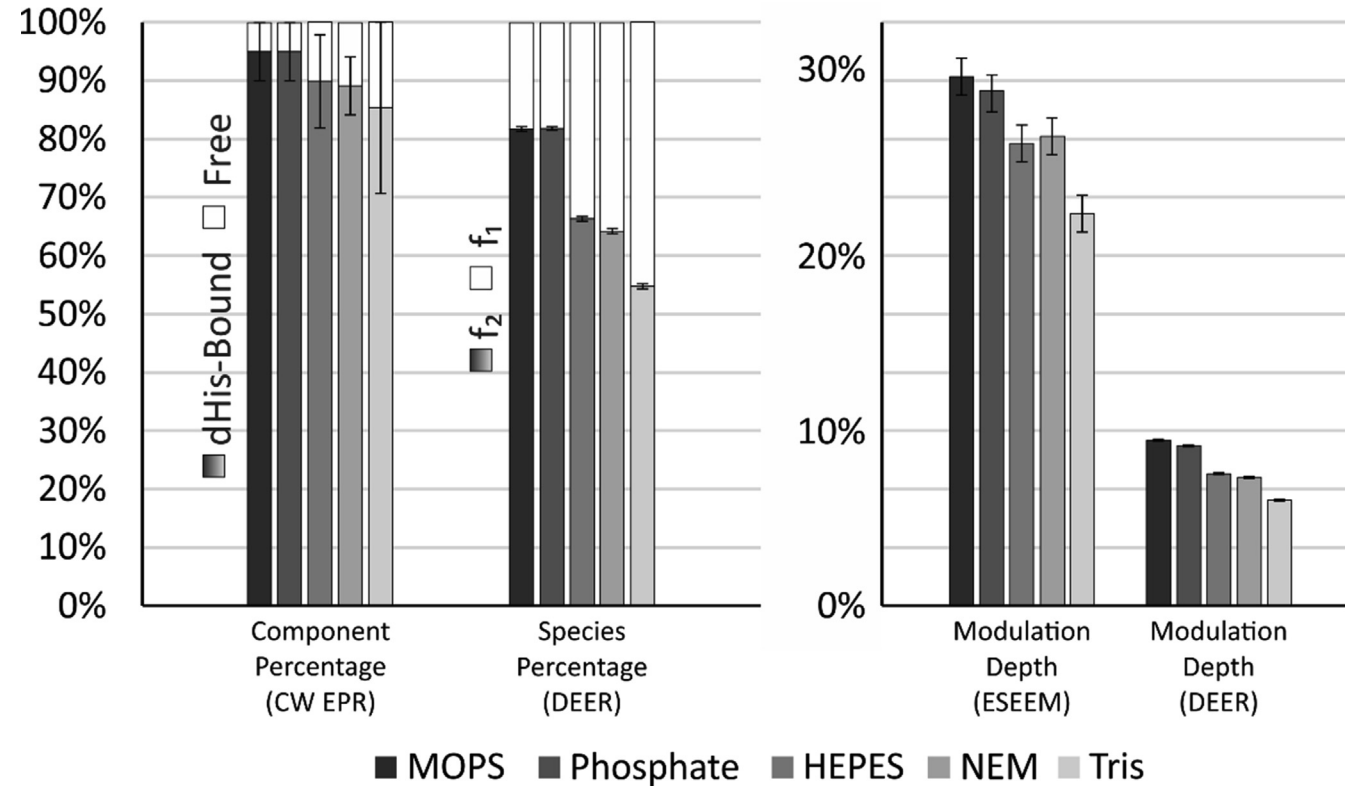

Fig. 10. Bar graph representing the major quantifiable values derived from our CW EPR, ESEEM and DEER experiments. The trends in these values provide a consistent picture of the loading of dHis sites across buffer systems. Note that f_1 includes both free Cu(II)-NTA as well as Cu(II)-NTA bound to one dHis site.

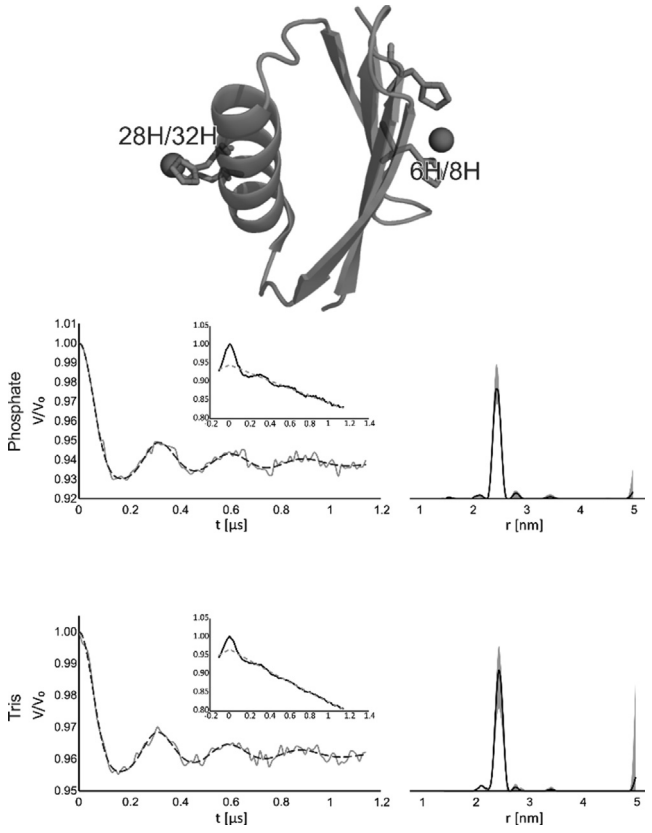

Fig. 11. Protein Structure of 6H/8H/28H/32H GB1 with dHis sites labeled (PDB: 4WH4), Above. DEER data for 100 μM protein in 50 mM sodium phosphate and Tris buffers prepared as described previously, Below.

modynamic trends suggest that the choice of buffer is an important consideration to make when implementing the dHis motif in new systems.

4. Conclusion

In this work, we have presented evidence that buffer conditions can affect the loading of Cu^{2+}-NTA into dHis sites for use with EPR distance methods. Our results indicate that sodium phosphate and MOPS buffers promote more efficient Cu^{2+}-NTA binding to the dHis sites, whereas Tris buffer degrades the loading efficiency. We have provided experimental control data of the expected results for each step in the labeling process used to achieve these results, most notably with regard to the incubation time and temperature of the protein and Cu^{2+}-NTA. We have demonstrated that maximal dHis loading can be achieved in less than 30 min at low temperature, which is an important consideration for protein research. Through this optimized labeling procedure, we show a 28% increase in doubly labeled protein compared to previously published results. When considering both the optimized loading protocol as well as ideal buffer conditions, we have achieved a fraction of doubly labeled proteins of up to ~80%. Our cumulative results provide new insights into considerations to be made when implementing the dHis Cu^{2+}-NTA system, and general optimized conditions for its use.

Declaration of Competing Interest

The authors declare that they have no known competing financial interests or personal relationships that could have appeared to influence the work reported in this paper.

Acknowledgments

Funding provided by NSF-BSF MCB-2006154.

References

[1] G. Jeschke, The Contribution of Modern EPR to Structural Biology, Emerg. Topics Life Sci. 2 (2018) 9–18.
[2] W.L. Hubbell, C. Altenbach, Investigation of Structure and Dynamics in Membrane Proteins Using Site-Directed Spin Labeling, Cur. Opin. Struct. Biol. 4 (1994) 566–573.
[3] W.L. Hubbell, H.S. McHaourab, C. Altenbach, M.A. Lietzow, Watching Proteins Move Using Site-Directed Spin Labeling, Structure 4 (1996) 779–783.
[4] L.J. Berliner, S.S. Eaton, G.R. Eaton, Distance Measurements in Biological Systems by EPR, Springer Sci. Business Media 19 (2006).
[5] T. Schmidt, M.A. Wälti, J.L. Baber, E.J. Hustedt, G.M. Clore, Long Distance Measurements up to 160 Å in the Groel Tetradecamer Using Q-Band Deer EPR Spectroscopy, Angew. Chem. Int. Ed. 55 (2016) 15905–15909.
[6] C. Altenbach, A.K. Kusnetzow, O.P. Ernst, K.P. Hofmann, W.L. Hubbell, High-Resolution Distance Mapping in Rhodopsin Reveals the Pattern of Helix Movement Due to Activation, Proc. Natl. Acad. Sci. 105 (2008) 7439–7444.
[7] R. Ward, M. Zoltner, L. Beer, H. El Mkami, I.R. Henderson, T. Palmer, D.G. Norman, The Orientation of a Tandem Potra Domain Pair, of the Beta-Barrel Assembly Protein Bama Determined by Peldor Spectroscopy, Structure 17 (2009) 1187–1194.
[8] V. Singh, M. Azarkh, T.E. Exner, J.S. Hartig, M. Drescher, Human Telomeric Quadruplex Conformations Studied by Pulsed EPR, Angew. Chem. Int. Ed. 48 (2009) 9728–9730.
[9] E.R. Georgieva, P.P. Borbat, C. Ginter, J.H. Freed, O. Boudker, Conformational Ensemble of the Sodium-Coupled Aspartate Transporter, Nat. Struct. Mol. Biol. 20 (2013) 215.
[10] I. Hänelt, D. Wunnicke, E. Bordignon, H.-J. Steinhoff, D.J. Slotboom, Conformational Heterogeneity of the Aspartate Transporter Gltph, Nat. Struct. Mol. Biol. 20 (2013) 210.
[11] O. Dalmas, P. Sompornpisut, F. Bezanilla, E. Perozo, Molecular Mechanism of Mg2+-Dependent Gating in Cora, Nat. Commun. 5 (2014) 3590.
[12] Z. Liu, T.M. Casey, M.E. Blackburn, X. Huang, L. Pham, I.M.S. de Vera, J.D. Carter, J.L. Kear-Scott, A.M. Veloro, L. Galiano, et al., Pulsed EPR Characterization of Hiv-1 Protease Conformational Sampling and Inhibitor-Induced Population Shifts, Phys. Chem. Chem. Phys. 18 (2016) 5819–5831.
[13] C.M. Grytz, A. Marko, P. Cekan, S.T. Sigurdsson, T.F. Prisner, Flexibility and Conformation of the Cocaine Aptamer Studied by Peldor, Phys. Chem. Chem. Phys. 18 (2016) 2993–3002.
[14] B. Verhalen, R. Dastvan, S. Thangapandian, Y. Peskova, H.A. Koteiche, R.K. Nakamoto, E. Tajkhorshid, H.S. McHaourab, Energy Transduction and Alternating Access of the Mammalian Abc Transporter P-Glycoprotein, Nature 543 (2017) 738.
[15] T.E. Assafa, K. Anders, U. Linne, L.-O. Essen, E. Bordignon, Light-Driven Domain Mechanics of a Minimal Phytochrome Photosensory Module Studied by EPR, Structure 26 (1534–1545) (2018) e4.
[16] H. Sameach, S. Ghosh, L. Gevorkyan-Airapetov, S. Saxena, S. Ruthstein, EPR Spectroscopy Detects Various Active State Conformations of the Transcriptional Regulator Cuer, Angew. Chem. Int. Ed. 58 (2019) 3053–3056.
[17] M.N. Kinde, Q. Chen, M.J. Lawless, D.D. Mowrey, J. Xu, S. Saxena, Y. Xu, P. Tang, Conformational Changes Underlying Desensitization of the Pentameric Ligand-Gated Ion Channel Elic, Structure 23 (2015) 995–1004.
[18] S.-Y. Park, P.P. Borbat, G. Gonzalez-Bonet, J. Bhatnagar, A.M. Pollard, J.H. Freed, A.M. Bilwes, B.R. Crane, Reconstruction of the Chemotaxis Receptor-Kinase Assembly, Nat. Struct. Mol. Biol. 13 (2006) 400–407.
[19] S.M. Hanson, E.S. Dawson, D.J. Francis, N. Van Eps, C.S. Klug, W.L. Hubbell, J. Meiler, V.V. Gurevich, A Model for the Solution Structure of the Rod Arrestin Tetramer, Structure 16 (2008) 924–934.
[20] H.A. DeBerg, J.R. Bankston, J.C. Rosenbaum, P.S. Brzovic, W.N. Zagotta, S. Stoll, Structural Mechanism for the Regulation of Hcn Ion Channels by the Accessory Protein Trip8b, Structure 23 (2015) 734–744.
[21] S. Valera, K. Ackermann, C. Pliotas, H. Huang, J.H. Naismith, B.E. Bode, Accurate Extraction of Nanometer Distances in Multimers by Pulse EPR, Chemistry – A European Journal 22 (2016) 4700–4703.
[22] D. Dawidowski, D.S. Cafiso, Munc18-1 and the Syntaxin-1 n Terminus Regulate Open-Closed States in a T-Snare Complex, Structure 24 (2016) 392–400.
[23] S. Milikisiyants, S. Wang, R.A. Munro, M. Donohue, M.E. Ward, D. Bolton, L.S. Brown, T.I. Smirnova, V. Ladizhansky, A.I. Smirnov, Oligomeric Structure of Anabaena Sensory Rhodopsin in a Lipid Bilayer Environment by Combining Solid-State NMR and Long-Range Deer Constraints, J. Mol. Biol. 429 (2017) 1903–1920.
[24] K.M. Stone, J.E. Townsend, J. Sarver, P.J. Sapienza, S. Saxena, L. Jen-Jacobson, Electron Spin Resonance Shows Common Structural Features for Different Classes of Ecori-DNA Complexes, Angew. Chem. Int. Ed. 47 (2008) 10192–10194.
[25] S. Ruthstein, M. Ji, P. Mehta, L. Jen-Jacobson, S. Saxena, Sensitive Cu2+-Cu2+ Distance Measurements in a Protein-DNA Complex by Dqc ESR, J. Phys. Chem. B. 117 (2013) 6227–6230.
[26] O. Duss, M. Yulikov, G. Jeschke, F.H. Allain, EPR-Aided Approach for Solution Structure Determination of Large Rnas or Protein-Rna Complexes, Nat. Commun. 5 (2014) 3669.
[27] H. Sameach, A. Narunsky, S. Azoulay-Ginsburg, L. Gevorkyan-Aiapetov, Y. Zehavi, Y. Moskovitz, T. Juven-Gershon, N. Ben-Tal, S. Ruthstein, Structural and Dynamics Characterization of the Merr Family Metalloregulator Cuer in Its Repression and Activation States, Structure 25 (2017) 988–996.
[28] J.E. Townsend, K. Stone, Z. Yang, J. Sarver, S. Saxena, L. Jen-Jacobson, The Enfolding Arms of Ecori Endonuclease as Probed by ESR Experiments, Biophys. J. 96 (2009) 63a.
[29] A.K. Upadhyay, P.P. Borbat, J. Wang, J.H. Freed, D.E. Edmondson, Determination of the Oligomeric States of Human and Rat Monoamine Oxidases in the Outer Mitochondrial Membrane and Octyl B-D-Glucopyranoside Micelles Using Pulsed Dipolar Electron Spin Resonance Spectroscopy, Biochemistry 47 (2008) 1554–1566.
[30] B.J. Gaffney, M.D. Bradshaw, S.D. Frausto, F. Wu, J.H. Freed, P. Borbat, Locating a Lipid at the Portal to the Lipoxygenase Active Site, Biophys. J. 103 (2012) 2134–2144.
[31] D.M. Yin, J.S. Hannam, A. Schmitz, O. Schiemann, G. Hagelueken, M. Famulok, Studying the Conformation of a Receptor Tyrosine Kinase in Solution by Inhibitor-Based Spin Labeling, Angew. Chem. Int. Ed. 56 (2017) 8417–8421.
[32] Z. Yang, M.R. Kurpiewski, M. Ji, J.E. Townsend, P. Mehta, L. Jen-Jacobson, S. Saxena, ESR Spectroscopy Identifies Inhibitory Cu^{2+} Sites in a DNA-Modifying Enzyme to Reveal Determinants of Catalytic Specificity, Proc. Natl. Acad. Sci. USA 109 (2012) E993–1000.
[33] D. Abdullin, N. Florin, G. Hagelueken, O. Schiemann, EPR-Based Approach for the Localization of Paramagnetic Metal Ions in Biomolecules, Angew. Chem. Int. Ed. 54 (2015) 1827–1831.
[34] E.G.B. Evans, M.J. Pushie, K.A. Markham, H.-W. Lee, G.L. Millhauser, Interaction between Prion Protein's Copper-Bound Octarepeat Domain and a Charged C-Terminal Pocket Suggests a Mechanism for N-Terminal Regulation, Structure 24 (2016) 1057–1067.
[35] W.L. Hubbell, C.J. López, C. Altenbach, Z. Yang, Technological Advances in Site-Directed Spin Labeling of Proteins, Curr. Opin. Struct. Biol. 23 (2013) 725–733.
[36] J.L. Sarver, J.E. Townsend, G. Rajapakse, L. Jen-Jacobson, S. Saxena, Simulating the Dynamics and Orientations of Spin-Labeled Side Chains in a Protein–DNA Complex, J. Phys. Chem. B 116 (2012) 4024–4033.
[37] K. Sale, L. Song, Y.-S. Liu, E. Perozo, P. Fajer, Explicit Treatment of Spin Labels in Modeling of Distance Constraints from Dipolar EPR and Deer, J. Am. Chem. Soc. 127 (2005) 9334–9335.
[38] R.M. Lösel, R. Philipp, T. Kálai, K. Hideg, W.E. Trommer, Synthesis and Application of Novel Bifunctional Spin Labels, Bioconjug. Chem. 10 (1999) 578–582.
[39] I.D. Sahu, R.M. McCarrick, K.R. Troxel, R. Zhang, H.J. Smith, M.M. Dunagan, M.S. Swartz, P.V. Rajan, B.M. Kroncke, C.R. Sanders, et al., Deer EPR Measurements for Membrane Protein Structures Via Bifunctional Spin Labels and Lipodisq Nanoparticles, Biochemistry 52 (2013) 6627–6632.
[40] R.F. Rayes, T. Kálai, K. Hideg, M.A. Geeves, P.G. Fajer, Dynamics of Tropomyosin in Muscle Fibers as Monitored by Saturation Transfer EPR of Bi-Functional Probe, PLoS ONE 6 (2011) e21277.
[41] M.R. Fleissner, M.D. Bridges, E.K. Brooks, D. Cascio, T. Kálai, K. Hideg, W.L. Hubbell, Structure and Dynamics of a Conformationally Constrained Nitroxide Side Chain and Applications in EPR Spectroscopy, Proc. Natl. Acad. Sci. 108 (2011) 16241–16246.
[42] T.F. Cunningham, M.R. Putterman, A. Desai, W.S. Horne, S. Saxena, The Double-Histidine Cu2+-Binding Motif: A Highly Rigid, Site-Specific Spin Probe for Electron Spin Resonance Distance Measurements, Angew. Chem. Int. Ed. 54 (2015) 6330–6334.
[43] M.J. Lawless, S. Ghosh, T.F. Cunningham, A. Shimshi, S. Saxena, On the Use of the Cu2+–Iminodiacetic Acid Complex for Double Histidine Based Distance Measurements by Pulsed ESR, Phys. Chem. Chem. Phys. 19 (2017) 20959–20967.
[44] S. Ghosh, M.J. Lawless, G.S. Rule, S. Saxena, The Cu2+-Nitrilotriacetic Acid Complex Improves Loading of A-Helical Double Histidine Site for Precise Distance Measurements by Pulsed ESR, J. Magn. Reson. 286 (2018) 163–171.
[45] M.J. Lawless, J.R. Pettersson, G.S. Rule, F. Lanni, S. Saxena, ESR Resolves the C Terminus Structure of the Ligand-Free Human Glutathione S-Transferase A1–1, Biophys. J . 114 (2018) 592–601.
[46] A. Gamble Jarvi, T.F. Cunningham, S. Saxena, Efficient Localization of a Native Metal Ion within a Protein by Cu2+-Based EPR Distance Measurements, Phys. Chem. Chem. Phys. 21 (2019) 10238–10243.
[47] A. Gamble Jarvi, K. Ranguelova, S. Ghosh, R.T. Weber, S. Saxena, On the Use of Q-Band Double Electron-Electron Resonance to Resolve the Relative Orientations of Two Double Histidine-Bound Cu2+ Ions in a Protein, J. Phys. Chem. B 122 (2018) 10669–10677.
[48] Singewald, K.; Bogetti, X.; Sinha, K.; Rule, G.; Saxena, S. K. Double Histidine Based EPR Measurements at Physiological Temperatures Permit Site-Specific Elucidation of Hidden Dynamics in Enzymes. Angewandte Chemie International Edition 10.1002/anie.202009982.
[49] R.J.P. Williams, Metal Ions in Biological Systems, Biol. Rev. 28 (1953) 381–412.
[50] C.M.H. Ferreira, I.S.S. Pinto, E.V. Soares, H.M.V.M. Soares, (Un)Suitability of the Use of Ph Buffers in Biological, Biochemical and Environmental Studies and Their Interaction with Metal Ions – a Review, RSC Adv. 5 (2015) 30989–31003.
[51] M.R. Mehlenbacher, F. Bou-Abdallah, X.X. Liu, A. Melman, Calorimetric Studies of Ternary Complexes of Ni(II) and Cu(II) Nitrilotriacetic Acid and N-Acetyloligohistidines, Inorg. Chim. Acta 437 (2015) 152–158.

[52] T.F. Cunningham, M.S. McGoff, I. Sengupta, C.P. Jaroniec, W.S. Horne, S. Saxena, High-Resolution Structure of a Protein Spin-Label in a Solvent-Exposed B-Sheet and Comparison with Deer Spectroscopy, Biochemistry 51 (2012) 6350–6359.
[53] T.F. Cunningham, S. Pornsuwan, W.S. Horne, S. Saxena, Rotameric Preferences of a Protein Spin Label at Edge-Strand B-Sheet Sites, Protein Sci. 25 (2016) 1049–1060.
[54] S. Stoll, A. Schweiger, Easyspin, a Comprehensive Software Package for Spectral Simulation and Analysis in EPR, J. Magn. Res. 178 (2006) 42–55.
[55] W.B. Mims, Envelope Modulation in Spin-Echo Experiments, Physical Review B 5 (1972) 2409–2419.
[56] J.M. Fauth, A. Schweiger, L. Braunschweiler, J. Forrer, R.R. Ernst, Elimination of Unwanted Echoes and Reduction of Dead Time in Three-Pulse Electron Spin-Echo Spectroscopy, J. Magn. Reson. 1986 (66) (1969) 74–85.
[57] M. Pannier, S. Veit, A. Godt, G. Jeschke, H.W. Spiees, Dead-Time Free Measurement of Dipole-Dipole Interactions between Electron Spins, J. Magn. Reson. 142 (2000) 331–340.
[58] A. Milov, A. Maryasov, Y.D. Tsvetkov, Pulsed Electron Double Resonance (Peldor) and Its Applications in Free-Radicals Research, Appl. Magn. Reson. 15 (1998) 107–143.
[59] G. Jeschke, V. Chechik, P. Ionita, A. Godt, H. Zimmermann, J. Banham, C.R. Timmel, D. Hilger, H. Jung, Deeranalysis 2006—a Comprehensive Software Package for Analyzing Pulsed Eldor Data, Appl. Magn. Reson. 30 (2006) 473–498.
[60] L. Harju, R. Sara, Spectrophotometric Titrations of Nitrilotriacetic Acid with Copper(II) as Monoligand and Biligand Chelates, Anal. Chim. Acta 73 (1974) 129–139.
[61] V.S. Sergienko, Specific Structural Features of Copper(II) Complexonates with Nitrilotriacetate Anions: A Review, Crystallogr. Rep. 51 (2006) 236–257.
[62] J. Peisach, W.E. Blumberg, Structural Implications Derived from the Analysis of Electron Paramagnetic Resonance Spectra of Natural and Artificial Copper Proteins, Arch. Biochem. Biophys. 165 (1974) 691–708.
[63] Anderegg, G. Critical Survey of Stability Constants of Nta Complexes. 1982, 54, 2693.
[64] Sjöberg, S. Critical Evaluation of Stability Constants of Metal-Imidazole and Metal-Histamine Systems (Technical Report). 1997, 69, 1549.
[65] D. Pyreu, M. Bazanova, Thermodynamics of Mixed-Ligand Complex Formation of Metal (II) Complexonates with Imidazole in Aqueous Solution, Inorg. Chim. Acta 453 (2016) 687–691.
[66] S.A. Dikanov, Y. Tsvetkov, Electron Spin Echo Envelope Modulation (Eseem) Spectroscopy, CRC Press, 1992.
[67] J.L. Wort, K. Ackermann, A. Giannoulis, A.J. Stewart, D.G. Norman, B.E. Bode, Sub-Micromolar Pulse Dipolar EPR Spectroscopy Reveals Increasing Cuii-Labelling of Double-Histidine Motifs with Lower Temperature, Angew. Chem. Int. Ed. 58 (2019) 11681–11685.
[68] E. Bernarducci, P.K. Bharadwaj, K. Krogh-Jespersen, J.A. Potenza, H.J. Schugar, Electronic Structure of Alkylated Imidazoles and Electronic Spectra of Tetrakis (Imidazole)Copper(II) Complexes. Molecular Structure of Tetrakis(1,4,5-Trimethylimidazole)Copper(II) Diperchlorate, J. Am. Chem. Soc. 105 (1983) 3860–3866.
[69] P. Thordarson, Determining Association Constants from Titration Experiments in Supramolecular Chemistry, Chem. Soc. Rev. 40 (2011) 1305–1323.
[70] J.E.A. Webb, M.J. Crossley, P. Turner, P. Thordarson, Pyromellitamide Aggregates and Their Response to Anion Stimuli, J. Am. Chem. Soc. 129 (2007) 7155–7162.
[71] L. Kevan, Modulation of Electron Spin-Echo Decay in Solids, Time Domain Electron Spin Resonance (1979) 279–341.
[72] B.-K. Shin, S. Saxena, Substantial Contribution of the Two Imidazole Rings of the His13−His14 Dyad to Cu(II) Binding in Amyloid-B(1–16) at Physiological Ph and Its Significance, J. Phys. Chem. A 115 (2011) 9590–9602.
[73] K.I. Silva, B.C. Michael, S.J. Geib, S. Saxena, Eseem Analysis of Multi-Histidine Cu(II)-Coordination in Model Complexes, Peptides, and Amyloid-B, J. Phys. Chem. B 118 (2014) 8935–8944.
[74] Z. Yang, M. Ji, S. Saxena, Practical Aspects of Copper Ion-Based Double Electron Electron Resonance Distance Measurements, Appl. Magn. Reson. 39 (2010) 487–500.
[75] Borbat, P. P.; Freed, J. H., Pulse Dipolar Electron Spin Resonance: Distance Measurements. In Structural Information from Spin-Labels and Intrinsic Paramagnetic Centres in the Biosciences, Timmel, C. R.; Harmer, J. R., Eds. Springer Berlin Heidelberg: Berlin, Heidelberg, 2013; pp 1-82.
[76] L. Bologni, A. Sabatini, A. Vacca, Complex Formation Equilibria between 2-Amino-2(Hydroxymethyl)-1,3,-Propanediol (Tris, Tham) and Nickel(II), Copper (II), Zinc(II) and Hydrogen Ions in Aqueous Solutions, Inorg. Chim. Acta 69 (1983) 71–75.
[77] Z.M. Anwar, H.A. Azab, Ternary Complexes in Solution. Comparison of the Coordination Tendency of Some Biologically Important Zwitterionic Buffers toward the Binary Complexes of Some Transition Metal Ions and Some Amino Acids, J. Chem. Eng. Data 44 (1999) 1151–1157.
[78] K.J. Powell, P.L. Brown, R.H. Byrne, T. Gajda, G. Hefter, S. Sjöberg, H. Wanner, Chemical Speciation of Environmentally Significant Metals with Inorganic Ligands Part 2: The Cu2+-Oh-, Cl-, Co32-, So42-, and Po43-, Systems (Iupac Technical Report) 79 (2007) 895.